Semi-Empirical Model of Nickel Manganese Cobalt (NMC) Lithium-Ion Batteries Including Capacity Regeneration Phenomenon

Bodnar, David; Mouli, Gautham Ram Chandra; Durovsky, Frantisek; Bauer, Pavol; Qin, Zian

DOI
10.1109/TTE.2024.3396277

Publication date
2025

Document Version
Final published version

Published in
IEEE Transactions on Transportation Electrification

Citation (APA)
Bodnar, D., Mouli, G. R. C., Durovsky, F., Bauer, P., & Qin, Z. (2025). Semi-Empirical Model of Nickel Manganese Cobalt (NMC) Lithium-Ion Batteries Including Capacity Regeneration Phenomenon. *IEEE Transactions on Transportation Electrification* , *11*(1), 797-813. https://doi.org/10.1109/TTE.2024.3396277

Semi-Empirical Model of Nickel Manganese Cobalt (NMC) Lithium-Ion Batteries Including Capacity Regeneration Phenomenon

Dávid Bodnár, Gautham Ram Chandra Mouli, *Member, IEEE*, František Ďurovský,
Pavol Bauer, *Senior Member, IEEE*, and Zian Qin, *Senior Member, IEEE*

***Abstract*— The development of lithium-ion batteries has experienced massive progress in recent years. Battery aging models are employed in advanced battery management systems (BMSs) to optimize the use of the battery and prolong its lifetime. However, Li-ion battery cells often experience fluctuations in battery capacity and performance during cycling, which makes capacity prediction more difficult. Moreover, the reason for the capacity regeneration phenomenon occurring after resting periods is not clear yet, as well as the influence of cycling conditions on capacity regeneration. A relationship between this phenomenon to cycling state of charge (SoC) ranges and current rates was investigated in this article on a battery cell with lithium nickel manganese cobalt (NMC) oxide positive electrode. Experimental results show that the capacity increase is a consequence of decreased internal impedance after the resting period. The experiments also showed that a significant power drop and subsequent power regeneration after a resting period occurs only for specific SoC ranges, and applying a resting period after battery cycling can mitigate this power fading process. The semi-empirical model of battery degradation including capacity regeneration is proposed in this article based on physical processes inside of the cell retaining low computational requirements. The acquired results can be utilized in BMSs for more accurate state of health (SoH) estimation and to prolong battery lifetime.**

***Index Terms*— Aging, batteries, modeling.**

I. INTRODUCTION

ELECTRIC mobility has gained more popularity in recent years due to its lower environmental impact, high efficiency, lower total cost of ownership, and great potential for improvement compared to internal combustion engine vehicles. However, mass adoption of electric mobility is still hindered by obstacles, one of which is the high price, limited cycle life the degradation of the lithium-ion (Li-ion) battery. There are more methods to lower battery degradation, the most important ones are an integration of an active thermal management system, which ensures moderate temperatures of the battery pack during operation, and a battery management system (BMS) [1]. BMS ensures the safe and reliable operation of the pack. It specifically performs temperature measurements, cell balancing, overcharge and overdischarge protection, state of charge (SoC) and state of health (SoH) estimation, power limits calculation, and more [2]. Advanced BMS is equipped with a battery model, which plays a critical role in providing valuable information on the performance and condition of the battery, which enables efficient and safe management. The goal of battery modeling is to predict battery behavior under different operating conditions and optimization of BMS performance to extend battery life [3].

A. Literature Review

A battery cell is an electrochemical system and the behavior of a battery is influenced by a wide range of factors, which makes battery modeling a complex and challenging task. Understanding the relationship between electrical, chemical, and mechanical processes is crucial for developing a reliable battery model. As a result, battery models rely on a combination of experimental data and mathematical equations to predict the behavior of the battery. There are several types of battery models, e.g., empirical models, semi-empirical models, electrochemical models, physics-based models, or data-driven models [4], [5], [6], [7]. Empirical models are based on experimental measurements, they are relatively simple but suffer from lower adaptability.

On the other hand, electrochemical models are expressed in the form of nonlinear partial differential equations, which are characterized by high accuracy, but also by large computational requirements [8]. One of the requirements on battery models applied in BMS is low processing power. This generally prevents the use of electrochemical models in electric vehicle (EV) applications [9]. Therefore, a trade-off between accuracy and low computational power must be found. One of the options is to use physics-based models, which are simpler compared to electrochemical models and allow insight into electrochemical behaviors, which equivalent

Manuscript received 11 January 2024; revised 27 March 2024; accepted 17 April 2024. Date of publication 2 May 2024; date of current version 3 February 2025. This work was supported by Slovak Research and Development Agency under Contract APVV-18-0436 and in part by the Scientific Grant Agency of the Ministry of Education of the Slovak Republic under Project VEGA 1/0363/23 and Project VEGA 1/0584/24. *(Corresponding author: Zian Qin.)*

Dávid Bodnár and František Ďurovský are with the Department of Electrical Engineering and Mechatronics, Technical University of Košice, 040 01, Košice, Slovakia (e-mail: david.bodnar@tuke.sk; frantisek.durovsky@tuke.sk).

Gautham Ram Chandra Mouli, Pavol Bauer, and Zian Qin are with the Department of Electrical Sustainable Energy, DCE&S Group, TU Delft, 2628 CD Delft, The Netherlands (e-mail: G.R.ChandraMouli@tudelft.nl; P.Bauer@tudelft.nl; Z.Qin-2@tudelft.nl).

Digital Object Identifier 10.1109/TTE.2024.3396277

circuit models (ECMs) cannot do. ECMs can also exhibit very high accuracy, terminal voltage predictions can be equally accurate compared to electrochemical models in some cases.

Battery aging is a very complex process, which can be caused by a number of reasons, such as lithium plating, growth of the solid electrolyte interphase (SEI) layer, transition metal dissolution, mechanical cracking, electrolyte depletion, and others. These degradation mechanisms are usually interacting and do not work in isolation. For example, SEI growth can exacerbate the rate of lithium plating [10], or graphite particle cracking causes further SEI growth [11]. Modeling all degradation mechanisms is not practically possible, however, understanding the most significant mechanisms is important for implementing sufficiently accurate battery models. The ones with the greatest influence are described in Appendix A.

In addition, battery aging depends on a wide range of often interacting factors. Despite various studies observing SoC, depth of discharge (DoD) change ΔDoD (the definition of the terms SoC, DoD, and ΔDoD can be found in Appendix B of this article), C-rate (the rate at which the cell is charged or discharged relative to its nominal capacity), and temperature dependency on battery aging, satisfactory conclusions regarding SoC and ΔDoD cannot be drawn yet [12]. The reason is that most of the conducted tests were made only for a few specific ranges of SoC, respectively, ΔDoD, and not enough data were available to establish sufficiently precise relationships. Less attention was also paid to investigating physical processes causing diverse degradation across the whole SoC range. Moreover, several studies were carried out under accelerated aging conditions such as high temperatures up to 60 °C and high C-rate [11], [13], [14], [15]. The results could thus be influenced by several different degradation processes, which lead to problems with their decoupling and create very demanding modeling.

Moreover, Li-ion cells often experience the so-called capacity regeneration phenomenon [16], [17], [18], [19], [20]. After a resting period is applied to a previously cycled cell, the measured capacity is higher than the capacity of the previous cycle. This observation cannot be explained by the temperature change of the cell because after the resting period, the cell temperature is lower or the same as at the end of the cycling. The lower temperature would cause a decrease in the measured capacity, not an increase.

B. Research Gaps

The scientific community did not extensively focus on the research of the capacity regeneration phenomenon even though it has a huge impact on battery performance. The reason for this behavior has not been sufficiently explained in the literature yet. Eddahech et al. [16] and [17], that it might be related to charge redistribution during the resting period, but no further explanation was given. Based on [18], capacity fluctuation correlates with polarization recovery because the resting time allows particles to spread evenly. In [20], the Li-ion battery performance under low temperatures was studied, where the capacity regeneration was observed. However, several degradation mechanisms were found during postmortem analysis like lithium plating, the anode material detached from the copper foil, or cracks between the cathode primary particles. Epding et al. [21] also observed capacity regeneration and ruled out the anode overhang effect as a possible reason for this behavior. They proposed the reactivation of passivated metallic lithium plating as an explanation, which was based on voltage relaxation tests indicating lithium plating. However, more degradation mechanisms might have been present there and this hypothesis was not proven yet. Therefore, the exact reason for the capacity regeneration is not clear. More information about this phenomenon is needed for understanding and modeling battery behavior, and the potential extension of battery lifetime.

Regarding the capacity regeneration modeling, there were efforts to describe this behavior in [18], [19], [22], [23], [24], [25], and [26] using different methods, e.g. hybrid ensemble learning model [18], expectation maximization-unscented particle filter Wilcoxon rank sum test approach [26], long short-term memory recurrent network [19], or autoregressive model and particle filter algorithm [23]. However, most of these studies were using the NASA Ames Prognostic Center of Excellence dataset for modeling and also for model verification, where data from only four tested cells were used. These works have not investigated the influence of average SoC, ΔDoD, or C-rate. Furthermore, they all use only data on the measured discharge capacity and do not consider the impact of the internal impedance of the cell.

C. Contributions

This article presents the following contributions:

1) The influence of different factors such as SoC, ΔDoD, and C-rate is investigated and explained from a physical point of view. The capacity regeneration phenomenon is observed for several cells cycled under different cycling conditions, and its relation to these factors is analyzed.
2) A semi-empirical battery aging model including the regeneration phenomenon based on changes in ECM parameters is proposed in this article. It was shown in this study that the capacity regeneration phenomenon is a consequence of internal impedance fluctuations. There is no apparent reason for fluctuations in the total battery capacity, so fluctuations in the discharge capacity are caused by varying internal impedance. Thus, the internal impedance model must be included to model the regeneration phenomenon. Therefore, the proposed model consists of the capacity fading model extended by the power fading model. We found out that the biggest influence on the regeneration phenomenon is the R_1 parameter of the ECM (the resistance related to the longer time constant caused by slow diffusion). Thus, a semi-empirical model was created, which captures the evolution of the R_1 parameter and its influence on the discharge capacity. The model has shown good performance with the root mean square error (RMSE) of 3.82% and was verified with our cell data and with the NASA battery dataset.

This article is organized as follows. Section II explains the testing procedures. Section III describes the experimental

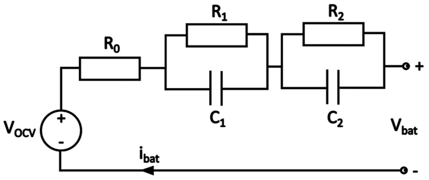

Fig. 1. Second-order ECM.

setup and shows experimental results. Section IV contains the battery model proposal. In the end, the conclusion and discussion are contained in Section V.

II. Methodology

For battery modeling purposes, the ECM is the most popular one among many battery models used in the industry because of its low computational requirements. The dynamic behavior of the battery is described by resistance–capacitor (*RC*) pairs, where *RC* pairs represent physical processes inside the cell with different time constants [6]. The effect of SEI, charge transfer, and double layer effect is described by high-frequency *RC* pairs. Warburg impedance represents the diffusion process at low frequencies and is caused by diffusion inside the anode and cathode material and in a liquid electrolyte [27]. An infinite number of *RC* pairs is needed to accurately describe Warburg impedance [28]. However, due to practical constraints only a limited number of *RC* pairs is used for modeling purposes [27].

The second-order ECM is employed in this article. It consists of a voltage source, which is a function of SoC, an equivalent series resistor (ESR), and two *RC* pairs (see Fig. 1). ESR represents several contributions such as electrolyte resistance, separator, current collector, and electric conductivity of the active material [5].

Since the long-time constants are the most important in EV applications and other energy storage system (ESS) applications, the ECM is often modeled with two *RC* pairs describing the Warburg impedance (parameters R_1, C_1, R_2, C_2), and other processes (with frequency > 1 Hz) are included in the series resistance parameter (R_0) [6], [28].

There are several methods for ECM parameter identification. The electrochemical impedance spectroscopy test procedure can be used, but it requires specific instrumentation. A hybrid pulse power characterization test can be used as well [29], however, 30 s of rest might not be sufficient. In [30], [31], [32], and [33], longer resting periods were applied in a pulse current test. Therefore, a parameter identification procedure described in [31] was adopted in this article. All important equations for the ECM parameters calculation can be also found in Appendix C.

A. Testing Procedure

The objective of the experiments is an observation of capacity fading and internal impedance changes for different SoC ranges, or C-rates respectively in order to create an accurate battery model. For battery testing and modeling, a high-energy density cylindrical Samsung INR18650-35E was used. The parameters of the cell are shown in Table I. The cell represents the nickel manganese cobalt (NMC) technology of Li-ion batteries, which is widely used in the automotive industry nowadays.

TABLE I
Parameters of INR18650-35E Cell

Capacity [Ah]	3.4	Max continuous discharge current [A]	8
Maximum voltage [V]	4.2	Max peak discharge current [A]	13
Nominal voltage [V]	3.6	Standard charge current [A]	1.7
Cut-off voltage [V]	2.65	Max charge current [A]	2
Useable energy [Wh]	12.06	Max power [W]	25.6
Weight [g]	50	Operating temperature [°C]	-10 to 60
Specific energy [Wh/kg]	241.2	Impedance at AC 1kHz [mΩ]	35

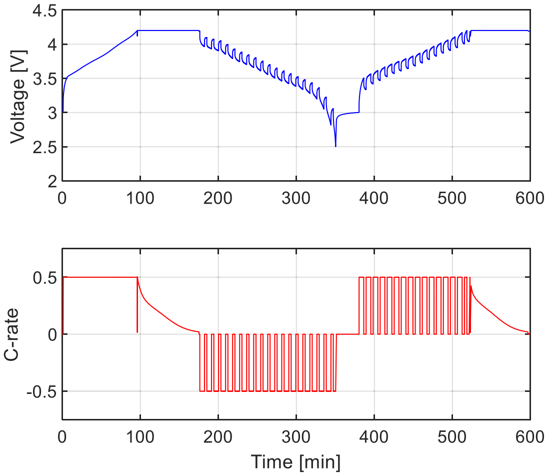

Fig. 2. Pulse current test.

Experiments consist of multiple capacity and internal impedance measurements and cycling tests. All tests are conducted at a room temperature of 25 °C. Before the cycling, a pulse current test and a capacity test are performed to obtain the initial parameters of the cell. The pulse current test (see Fig. 2) is employed for the extraction of ECM parameters. The cell is first charged by the standard constant current constant voltage (CCCV) method. The cell is charged by 0.5 C current until the maximum voltage of 4.2 V is reached, and subsequently charged by constant voltage until the charging current decreases below 0.02 C (68 mA). Then the cell is discharged by constant current by steps of 5% SoC at a C-rate of 0.5 C. The voltage response is measured for both discharging and charging across the whole SoC range (from 5% up to 95%). There is a resting period of 3 min between every two pulses, and the voltage response of this period is fit to obtain the ECM parameters.

The capacity test represents discharging a fully charged cell by the standard discharging current of 0.2 C until it reaches the cut-off voltage. Note that the capacity test measures the discharge capacity of the cell, which differs from the total capacity of the cell. The total capacity is the amount of charge when the cell is discharged from 100% SoC to 0%. The cell has internal impedance, which does not allow discharging the cell to 0% SoC. The larger the discharging C-rate and the

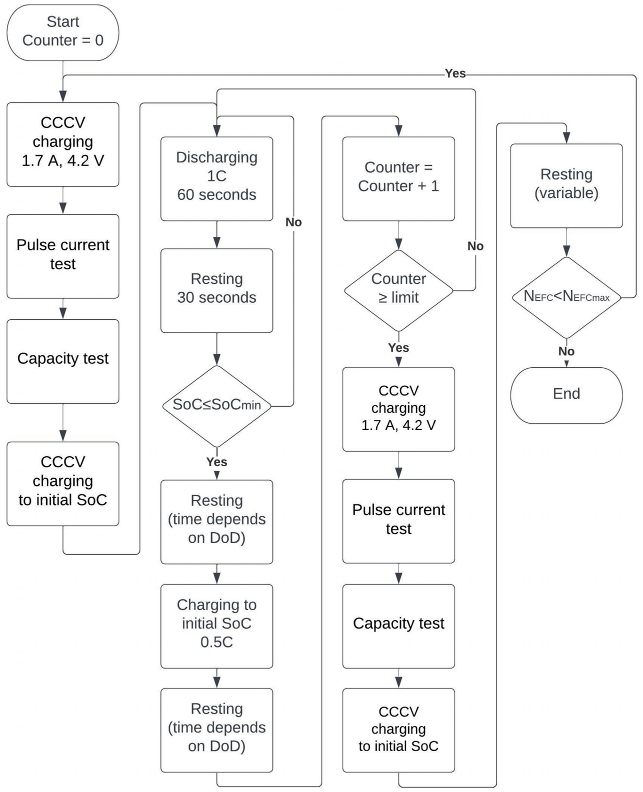

Fig. 3. Flowchart of the aging test procedure.

resistance parameters of ECM, the less portion of the total capacity is utilized. Therefore, the discharge capacity is always lower than the total capacity [34]. After every 25 equivalent full cycles (EFCs), the pulse current test and the capacity test are repeated.

The cycling procedure was arranged as follows (see Fig. 3). After the pulse current test and the capacity test, the cell was charged by the CCCV method to its initial voltage.

Then, a discharging current of 1 C (or 2 and 3 C for some of the tests) was applied for 60 s followed by 30 s of resting as shown in Fig. 3. Due to software limitations, the actual SoC value was not calculated, and the cell was always discharged by 340 mAh (for $\Delta\mathrm{DoD} = 10\%$), 1020 mAh ($\Delta\mathrm{DoD} = 30\%$), or 1700 mAh ($\Delta\mathrm{DoD} = 50\%$). The cell is consequently charged to the initial value of SoC by the standard charging current of 0.5 C (or 0.3 and 0.8 C for some of the tests).

There is a short resting period of 5 to 25 min between the charging and the discharging. The duration is not fixed the same for all cells because they were cycled with $\Delta\mathrm{DoD} = 10\%$, $\Delta\mathrm{DoD} = 30\%$, and $\Delta\mathrm{DoD} = 50\%$. The cells cycled with $\Delta\mathrm{DoD} = 10\%$ have to perform ten charge-discharge cycles to accomplish one EFC, but cells with $\Delta\mathrm{DoD} = 50\%$ only have two cycles. That means cells with $\Delta\mathrm{DoD} = 10\%$ experience more resting periods between charging and discharging. If the duration of the resting period was the same, the cells with $\Delta\mathrm{DoD} = 10\%$ would experience a longer testing time compared to other cells after the same amount of EFC. Therefore, the cells with $\Delta\mathrm{DoD} = 10\%$ will rest for 5 min, with $\Delta\mathrm{DoD} = 30\%$ for 15 min, and with $\Delta\mathrm{DoD} = 50\%$ for 25 min, so all the cells will accomplish the test roughly at the same time.

TABLE II

Cycle Aging Test Matrix for 1C Discharging Rate and 0.5C Charging Rate

ΔDoD [%]	10		30		50	
SoC range [%]	0-10	Cell 1	5-35	Cell 9	10-60	Cell13
	10-20	Cell 2	20-50	Cell10	20-70	Cell14
	20-30	Cell 3	30-60	Cell11		
	30-40	Cell 4	40-70	Cell12		
	40-50	Cell 5				
	50-60	Cell 6				
	60-70	Cell 7				
	70-80	Cell 8				

Since the cells with $\Delta\mathrm{DoD} = 10\%$ must perform more of these charge-discharging cycles to reach the same amount of EFC, the counter in Fig. 3 is set to finish cycling after the completion of 23 EFCs. Subsequently, the pulse current and the capacity tests are performed (two additional EFCs). After that, a variable resting phase is applied to investigate the capacity regeneration effect.

As mentioned above, different SoC ranges and ΔDoD were used for this procedure. However, the charging current must be restricted after reaching a voltage of 4.2 V (*CV* region), which under the standard charging current of 1.7 A occurs at SoC slightly higher than 80% depending on the internal impedance of the particular INR18650-35E cell. Battery aging and SEI growth highly depend on the C-rate of the charging current, which could negatively influence results aiming at SoC influence. To keep a uniform charging current for all cells, a cycle aging test matrix is proposed in Table II. This matrix allows testing multiple cells at the same ΔDoD with different average SoC.

B. OCV Test

The cycling tests consist of multiple pulse current and capacity tests. After every capacity test, the cell is charged to its initial voltage. To determine the initial voltage for different SoCs, the OCV test must be performed. The data from the OCV test can be later used also for OCV modeling.

The OCV test is usually performed analogically to the pulse current test at 0.5 C (see Fig. 2). The length of the resting time is also very important to measure the close-to-equilibrium OCV [30]. There are different suggested lengths across the literature. The resting time of 3 h was chosen because an error between the measured voltage and the OCV decays the most within the first few hours, so 3 h of resting can be regarded as a good trade-off between accuracy and time-consuming tests.

III. Experiments

For battery aging investigation, the cells must be cycled by a programmable current load. That is possible with the Arbin battery module tester, model LBT22043, which was used for all experiments (see Fig. 4). The tester contains 16 channels, and each provides a voltage range of 0–25 V and a current range of 0–10 A. The tester allows the paralleling of channels in case of higher current requirements. The battery

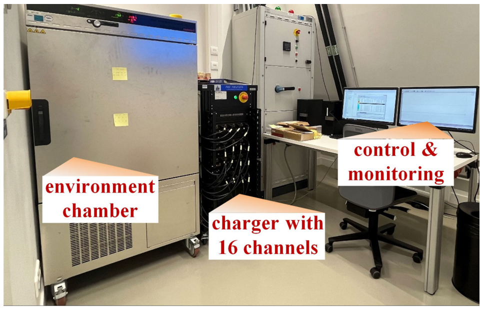

Fig. 4. Memmert environmental test chamber and Arbin battery module tester.

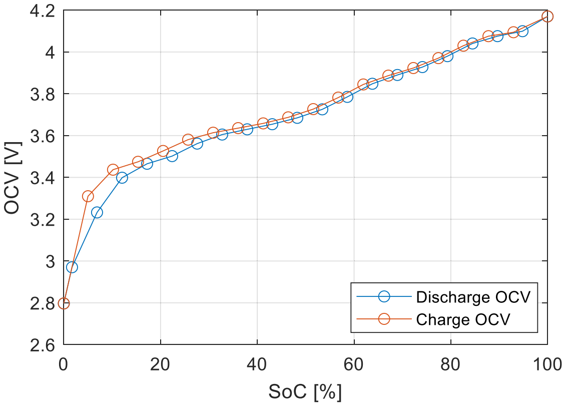

Fig. 5. OCV for discharging and charging of INR18650-35E.

cells were stored in Memmert environmental test chamber CTC256 with a programmable temperature range from −42 °C up to +190 °C. The difference between the cell surface and the temperature of the environmental chamber was very low, so the surface cell temperature was assumed to be equal to the temperature inside the chamber. Similarly, the temperature inside the cell was assumed to be the same as the cell surface temperature because measuring the temperature inside the cell is problematic for safety and practical reasons. The temperature difference between the cell surface and core at a discharging current of 1 C is for an 18 650 cell no more than 3 °C [35], [36].

A. OCV Test Results

Results of the OCV test are important for the identification of the voltage corresponding to specific SoC values. The results show differences between discharging and charging OCV, this hysteresis effect can be seen in Fig. 5. The value at 100% SoC was determined after 3 h of resting at the end of the charging process, and the value at 0% SoC at the end of the discharging process. The test was performed for three INR18650-35E cells with very little deviation. The charging OCV curve (red line in Fig. 5) was used for CCCV charging to the initial SoC (see Fig. 3). For modeling the dynamic behavior of the cell, the discharging OCV curve can be used during the discharging, and the charging OCV curve for the charging process to partially model battery hysteresis. The model is set to directly change from one OCV curve to another as the current polarity changes. However, fast dynamic changes were not studied in this article, and there was always a resting period of a few minutes between charging and discharging.

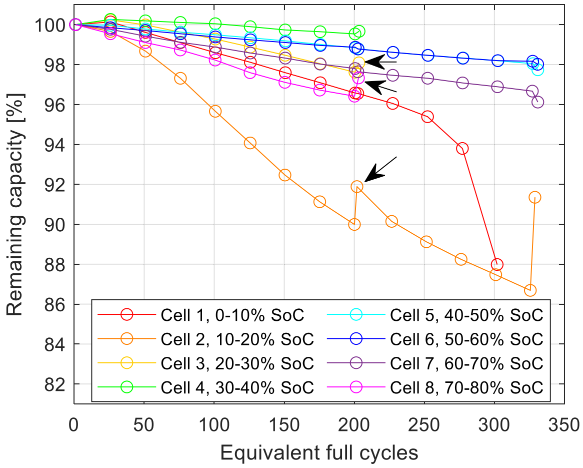

Fig. 6. Capacity fading of INR18650-35E cell for specific SoC ranges with 10% ΔDoD, regeneration is marked by arrows.

B. Experimental Results of Capacity Fading

Results of battery aging tests with respect to SoC are presented in Fig. 6. We can conclude that capacity fading has a linear character for most of the cells. The minimum degradation is observed for cells cycled between 30% and 40%, 40% and 50%, and 50% and 60% SoC, respectively. However, the cells cycled between 10% and 20%, 20% and 30%, and 70% and 80% SoC show distinct behavior with nonlinear character. Moreover, only these cells experienced significant capacity regeneration after a resting period marked by arrows in Fig. 6. The test was first stopped after 200 EFC and after three days of rest, it was restarted. The cycling of cells 3, 4, and 8 was interrupted after 200 EFC due to a software error, so the cycling did not continue for these cells. The test was stopped for the second time after 325 EFC with a resting period of 32 days. The most significant capacity increase was recorded for Cell 2 (10%–20% SoC). This cell also experienced the most capacity fade. After the first resting period, the capacity increased by 1.9%, and after the second by 4.6%. On the contrary, some of the cells recorded a slight decrease after resting, which was probably caused by a slightly higher temperature inside of the cell during cycling compared to the environmental chamber temperature, and the cell temperature dropped back to 25 °C after the resting period to match the environmental chamber temperature. In the case of modeling the temperature differences between the cell core and surface, an electro-thermal model can be used to describe the temperature behavior [37].

The cell cycled between 0% and 10% SoC experienced a sudden capacity drop after 250 EFC, which was caused by over-discharging of the cell. The cell was always discharged by 340 mAh from its initial SoC, which corresponds to a 10% discharge of a new cell. Since the cell experienced power and capacity fade, the cell experienced over-discharging in the later stages of cycling. Therefore, data points of Cell 1 after 250 EFC shall not be taken into account for modeling purposes.

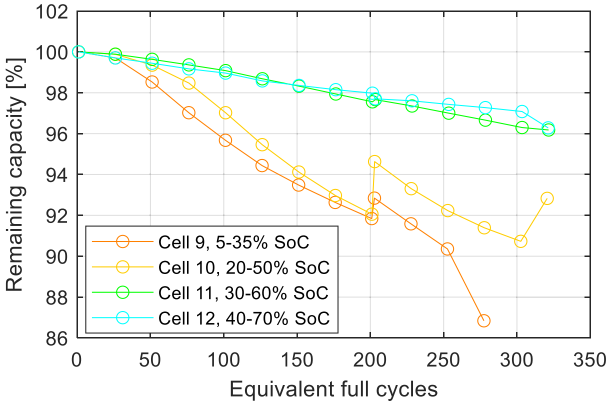

Fig. 7. Capacity fading of INR18650-35E cell for specific SoC ranges with 30% ΔDoD.

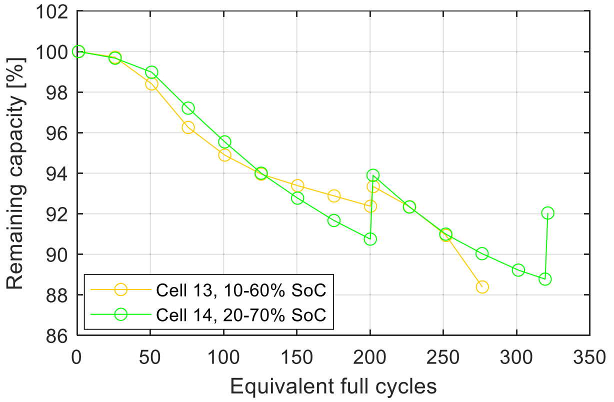

Fig. 8. Capacity fading of INR18650-35E cell for specific SoC ranges with 50% ΔDoD.

Similar results were observed for cells cycled at 30% ΔDoD, where Cell 11 and 12 indicate roughly linear behavior, whereas Cell 9 and 10 are strongly nonlinear including capacity regeneration (see Fig. 7). The same nonlinearity can be observed for Cell 13, and 14 as well where tests were done with 50% ΔDoD (see Fig. 8). Therefore, every cell which was cycled between 10% and 20% experienced a significant capacity drop and subsequent regeneration after the rest. This could indicate an additional degradation mechanism in this region. Since two different aging mechanisms appear to occur for INR18650-35E under standard conditions, the model will be divided into two parts, the first one representing linear behavior caused by SEI growth, and the second one representing the nonlinear effect of the regeneration phenomenon. Note that the SEI growth has also a square root of time dependence during the first several cycles, but then it shifts to linear time dependence [38]. This was observed in a number of different experimental studies [38], therefore, we will assume a linear SEI growth in long-term cycling.

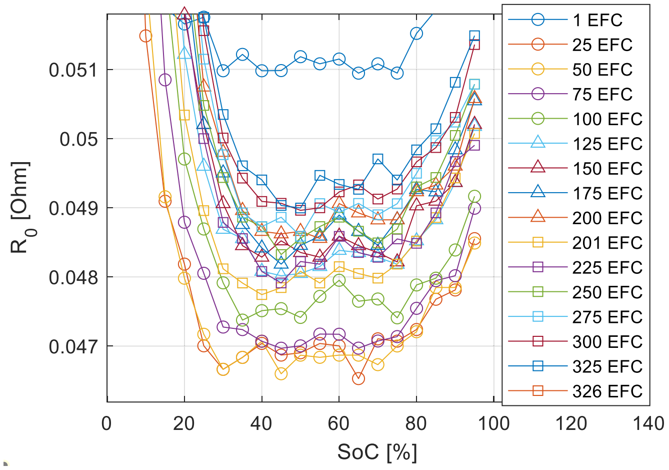

Fig. 9. Evolution of parameter R_0 of ECM of Cell 14.

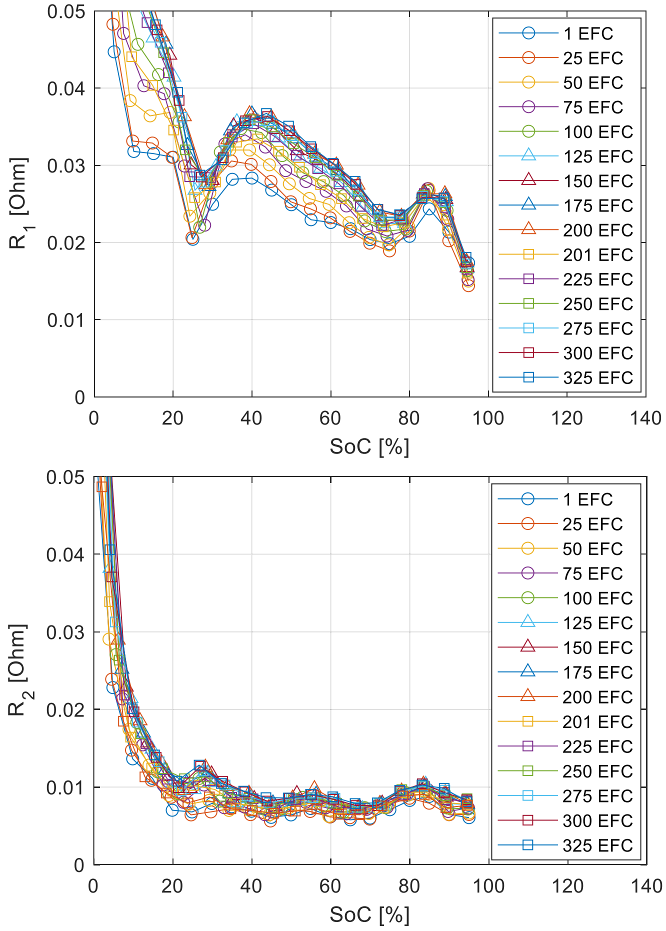

Fig. 10. Evolution of parameters R_1 and R_2 of ECM of Cell 14.

C. Experimental Results of Power Fading

Power fading of a cell results in a change of ECM parameters, which were determined based on the voltage response of the pulse current test. The evolution of parameters R_0, R_1, and R_2 of Cell 14 during aging as a function of SoC is shown in Figs. 9 and 10. The series resistance R_0 visibly dropped after the first cycles. The reason for this behavior is not clear, but one of the possible explanations is an enlargement of the graphite d-space during the early cycling stage, which separates the graphite layer structure. That results in a higher Li+ diffusion rate and lower internal resistance [39].

With further cycling, R_0 grows very slowly, and the R_0 growth did not exceed 2 mΩ. On the other side, the parameter R_1 recorded a relatively significant increase, which was varied

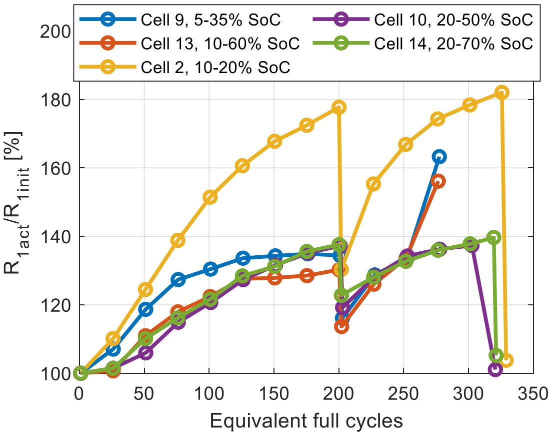

Fig. 11. Evolution of parameter R_1 at 50% SoC.

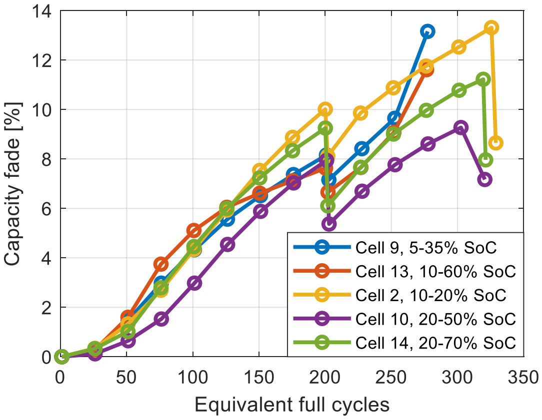

Fig. 12. Capacity fading of cells experiencing capacity and power regeneration.

with SoC (see Fig. 10). The R_1 growth indicates slower diffusion within electrode material with cell aging. The highest increase of R_1 was reported at lower SoC, on the contrary, the lowest changes were at higher SoC. This might be a result of higher concentration gradients in the later phase of the discharging pulse current test. There are also changes in the R_2 parameter shown in Fig. 10. Change of this parameter does not have a significant impact on the overall cell impedance with increasing EFC, and its value increased only by around 2 mΩ after 325 EFC. The R_2 growth is much smaller compared to the R_1 growth, which increased by around 10 mΩ after 325 EFC, so the R_1 growth had a much larger influence on power fading. Therefore, the evolution of the R_1 parameter will be investigated in more detail in this section. Note, that R_1 represents the RC pair with a longer time constant than R_2, so it can be concluded that slow diffusion processes are getting more important as the cell ages.

In order to quantify the increase of R_1 from EFC, the R_1 value for 50% SoC is taken and its increase is displayed in Fig. 11 with respect to the initial R_1 value. Cells 9, 13, 3, 10, and 14 were selected for Figs. 11 and 12 because they experienced the most significant R_1 growth.

The measured parameter R_1 converges to a certain value of R_1 with an increasing number of cycles, and R_1 drops sharply after applying a resting period. If a long enough resting period is applied, R_1 drops almost to its initial value. It indicates that capacity regeneration is a consequence of decreased diffusion, which reflects an increased resistance of R_1. Increased cell resistance causes an earlier decline of the cell voltage down to cut-off voltage, and a higher proportion of the battery energy being dissipated as heat. It means, that the whole cell capacity cannot be exploited at the same discharging C-rate.

A comparison of capacity fading and R_1 increase can be seen in Figs. 11 and 12. The capacity fading evolves in correlation with the parameter R_1. Since cell impedance has an impact on measured capacity as explained above, the assumption is that the change in parameter R_1 caused capacity regeneration in Fig. 12. However, after applying of long enough resting period, R_1 returns to its original value, whereas capacity does not because of the SEI growth. Therefore, the observed regeneration phenomenon can be recorded as power fading and power regeneration.

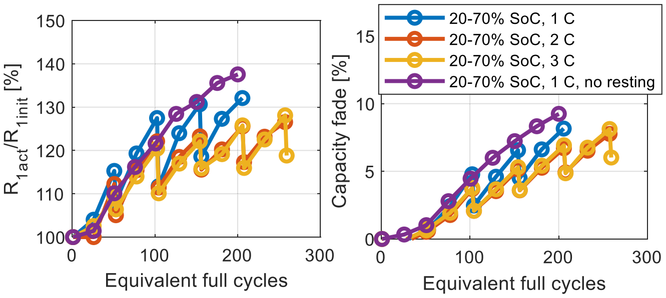

Fig. 13. R_1 parameter increase and capacity fade for discharging C-rates 1, 2, and 3 C at a fixed charging C-rate 0.5 C.

Other factors like temperature, charging C-rate, and discharging C-rate can also play a significant role. Power and capacity fading for different discharging C-rates are depicted in Fig. 13. C-rates of 1, 2, and 3 C were applied in this test, the charging current remained at the value of 0.5 C. A resting period of three days was applied after every 50 EFC. All cells were cycled between 20% and 70% SoC, and Cell 14 is also added to this figure as a reference, which did not experience any longer resting period (marked as "no resting"). The results show power fading for cells discharged by currents of 2 and 3 C is almost identical with very few differences. The cell discharged by 1 C shows a faster power and capacity fade. However, this cell shows a faster fading rate compared to Cell 14 already at the beginning of cycling before the first resting period. These two cells were cycled by the same current profile; therefore, the higher fading rate seems to be a consequence of a worse cycling ability of this particular cell, not a C-rate consequence. Thus, the discharging C-rate does not seem to have a significant effect on this specific cell's aging if the current stays within the maximum limits suggested by the manufacturer.

On the other hand, cells charged by a C-rate of 0.3, 0.5, and 0.8 C are depicted in Fig. 14 while maintaining a fixed discharging C-rate of 1 C. A strong dependence on charging C-rate is evident from these measurements. Moreover, power regeneration is much more significant for a higher charging C-rate. It can be therefore concluded, that lowering of charging current in the specific SoC region can effectively mitigate this degradation process.

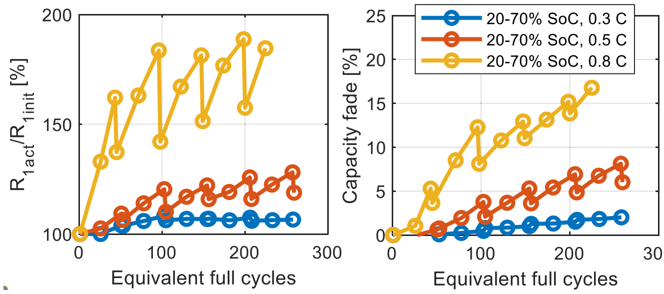

Fig. 14. R_1 parameter increase and capacity fade for charging C-rates 0.3, 0.5, and 0.8 C at a fixed discharging C-rate 1 C.

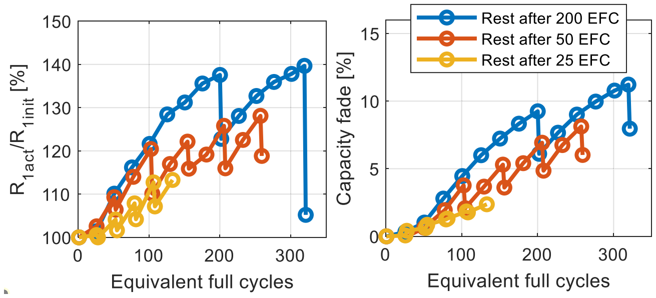

Fig. 15. R_1 parameter increase and capacity fade for cells resting after every 25, 50, and 200 EFC.

Another question to answer is the influence of the frequency of the resting period. In Fig. 15, results of three cells cycled between 20% and 70% SoC by charging current of 0.5 C are shown, where the first cell experienced the resting period after 200 EFC, the second after every 50 EFC, and the third after every 25 EFC. It is clear that the higher the frequency of resting, the lower the R_1 growth but also the lower R_1 regeneration.

The temperature effect also influences battery power fading. However, this study did not focus on different temperatures' impact on power fading and capacity regeneration, and it will be a subject of future studies.

D. Discussion About Reasons for the Regeneration Phenomenon

What still raises the question is the reason for the regeneration phenomenon. The R_1 parameter represents a resistance caused by concentration polarization or slow diffusion within electrode material respectively. Therefore, a possible explanation for the power fade and power regeneration could be a slower diffusion caused by mechanical strains within the electrode material. That creates larger concentration gradients, which can be observed as the R_1 increases, which results in an earlier drop of voltage down to the cut-off voltage, similarly as suggested in [18]. After a long resting time, concentration gradients are becoming lower creating the regeneration phenomenon as suggested in [17]. The mentioned mechanical strains can be an explanation for large differences in R_1 evolution for different SoC ranges.

Interesting is also the fact that the discharging C-rate seems to have a negligible effect on the R_1 growth as well as on the SEI growth (see Appendix D, where the influence of different factors on the SEI growth is explained). However, the SEI growth is unlikely to be the reason for the R_1 growth and regeneration since the SEI effect is observable in a high-frequency region (frequency $>$ 1 Hz) [6], [27], whereas the effect of R2 is at low frequencies (frequency $<$ 1 Hz). It also does not explain the regeneration phenomenon. On the other side, the mechanical strains within the electrode material during charging might be the reason for both faster SEI growth at higher charging C-rates and faster power fading due to slower diffusion and larger concentration gradients.

Another mechanism proposed to be related to the regeneration phenomenon in [21] is the reactivation of passivated metallic lithium plating. Lithium plating can be reversible and irreversible [40]. Reversible plating is stripped during the subsequent discharging or resting (so-called lithium stripping) [41], and this reversible part does not cause any capacity loss [40]. Only irreversible plating is responsible for the capacity losses. However, lithium plating is unlikely to occur during our experiments (excluding Cell 1) because lithium plating occurs under three possible operating conditions. These conditions are low-temperature charging, high charging C-rates, or charging at high SoC [42]. Most of the cells did not experience any of those conditions since the testing temperature was 25 °C, and the standard charging C-rate for INR18650-35E is 0.5 C.

Furthermore, a typical trend of capacity decay with lithium plating is different as observed in our experiments. In the case of lithium plating, a knee point is observed in the degradation behavior [12], [43]. After this point, the capacity starts steeply declining because the metallic lithium deposits on the anode, which reduces the active surface area resulting in a higher current density, and further increasing lithium plating [44]. On the other side, we observed a distinguished nonlinear behavior of a Li-ion cell due to the capacity regeneration phenomenon, and we did not observe a knee point typical for lithium plating. Therefore, to make sure that irreversible lithium plating did not occur in cells experiencing the regeneration phenomenon, Cell 2 and Cell 5 were selected for a postmortem analysis. Cell 2 was selected because the nonlinear behavior observed in our experiments (including capacity regeneration) was the most significant for this specific cell, which can be seen in Fig. 6. Cell 2 also experienced the most significant increase in the internal impedance (see Fig. 11), and the most significant capacity regeneration. Cell 5 was selected for comparison to Cell 2 because it did not experience nonlinear behavior and capacity regeneration. The postmortem analysis was made by disassembling the cells, and no signs of lithium plating were found on the anode of both cells under an electron microscope.

IV. PROPOSED BATTERY MODEL

The initial capacity of the cell gradually decreases due to cycling aging. The total battery capacity can be therefore calculated as

$$C_{\text{bat}} = C_{\text{init}} - \sum_{i=1}^{n} \Delta C_i \qquad (1)$$

where C_{init} is the initialization capacity at the beginning of life, ΔC_i is the capacity drop caused by cycling aging during the

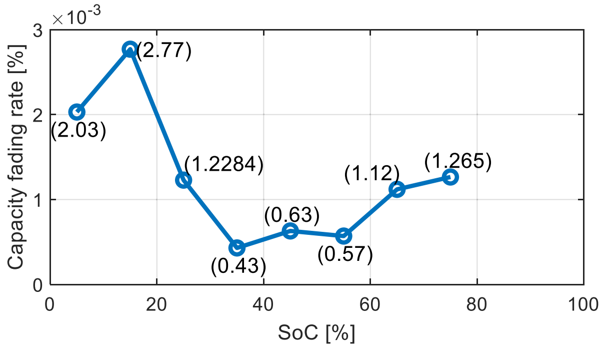

Fig. 16. Capacity fading rate as a function of average SoC.

ith cycle, and n is the number of cycles. For the cycling aging model, we will assume the main degradation processes: SEI growth and lithium plating [45]. ΔC_i can be then expressed as

$$\Delta C_i = \Delta C_{\mathrm{SEI}i} + \Delta C_{\mathrm{LP}i} \tag{2}$$

where $\Delta C_{\mathrm{SEI}i}$ stands for capacity loss caused by SEI growth during the ith cycle, and $\Delta C_{\mathrm{LP}i}$ is capacity loss by lithium plating during the ith cycle. Lithium plating was not investigated in this article and was not observed in our experiments as explained above. We can therefore assume $\Delta C_{\mathrm{LP}i}$ is equal to 0 in this case.

A. SEI Growth Modeling

For creating a semi-empirical model of capacity fading caused by SEI growth, a comprehension of physical phenomena happening inside the cell is needed. $\Delta C_{\mathrm{SEI}i}$ is a function of SoC, ΔDoD, C-rate, and temperature. The effect of each of those factors is discussed in Appendix D. The physical processes inside the cell are described there and provide an explanation for the construction of (4) to (7).

$\Delta C_{\mathrm{SEI}i}$ can be modeled as a product of four coefficients representing the impact of the four abovementioned effects

$$\Delta C_{\mathrm{SEI}i} = k_{\mathrm{SoC}i} k_{\mathrm{DoD}i} k_{Ii} k_{Ti} \tag{3}$$

where $k_{\mathrm{SoC}i}$ is a coefficient representing the SoC influence, $k_{\mathrm{DoD}i}$ coefficient representing ΔDoD influence, k_{Ii} C-rate influence, and k_{Ti} temperature impact. By using the product of these four coefficients, the model emphasizes the sensitivity of SEI growth and interdependency to multiple parameters simultaneously. A change in any of these factors could have a massive impact on the overall SEI growth so the multiplicative relationship was chosen.

We have received data about degradation for different SoC ranges with 10% ΔDoD (see Fig. 6). Function of capacity loss due to SEI growth from average SoC is depicted in Fig. 16. These values were obtained by linear polynomial function curve fitting of data in Fig. 6, where the slope represents the capacity fading rate. The linear function was applied to these data excluding the capacity regeneration. The coefficient $k_{\mathrm{SoC}i}$ can be then described as a definite integral of this function

$$k_{\mathrm{SoC}i} = \int_{\mathrm{SoC}L}^{\mathrm{SoC}H} f(\mathrm{SoC})d\mathrm{SoC} \tag{4}$$

TABLE III
Fit Parameters of Battery Model (Capacity Fading) for (4)–(6)

k_c	81.7e-6	k_d	2.6	k_e	1.222

where SoC_L is the SoC at the beginning of charging and SoC_H is the SoC at the end of charging. Another coefficient $k_{\mathrm{DoD}i}$ can be modeled by exponential function [46]

$$k_{\mathrm{DoD}i} = \left(1 + (k_d(\Delta\mathrm{DoD} - \Delta DoD_{\mathrm{ref}}))^{k_e}\right) \tag{5}$$

where k_d and k_e are fit constants, and $\Delta\mathrm{DoD}_{\mathrm{ref}}$ is a reference DoD, whereas in this case $\Delta\mathrm{DoD}_{\mathrm{ref}} = 0.1$. k_d and k_e could be also dependent on C-rate and temperature but determining the relation between them and ΔDoD impact requires further investigation.

Another influence on SEI growth is the C-rate. The impact of the C-rate on SEI growth was not tested in this study, but it is included in (3) as well as the temperature effect to provide an overall SEI growth model. SEI growth depends almost exclusively on charging current, so the impact of the discharging C-rate is neglected. For more information, see Appendix D. SEI growth is roughly proportional to charging C-rate, k_{Ii} is therefore,

$$k_{Ii} = k_c I_{\mathrm{char}} \tag{6}$$

where k_c is a fit constant and I_{char} is the charging current. C-rate has also some impact on the cell temperature, which accelerates SEI growth. SEI growth from temperature is described by Arrhenius equation

$$k_{Ti} = e^{-\frac{E_a}{R}\left(\frac{1}{T}-\frac{1}{T_{\mathrm{ref}}}\right)} \tag{7}$$

where T_{ref} stands for reference temperature 25°, T is the cell temperature measured at the surface, E_a is the activation energy, which is the minimum required energy to undergo a chemical reaction, and R stands for universal gas constant. The fit parameters of the capacity fading battery model are listed in Table III. For parameter identification, data from Cell 1 to 14 were used. Parameter E_a was not fit because all cells were tested at 25 °C, so k_{Ti} equals 1.

B. Modeling of Power Fade

The SEI growth can explain the linear behavior of the cells. However, there were many cells, which experienced strongly nonlinear capacity fading. This mechanism has also an influence on the internal impedance of the cell. Parameter R_1 increases at the beginning of cycling, but after several cycles, it converges to a specific value of R_1 until it reaches its steady state (see Fig. 11), which is visible, especially for Cell 9. R_1 growth without resting periods could be therefore modeled by a first-order system with time delay

$$R_{1\mathrm{act}} = R_{1\mathrm{init}}\left(1+\frac{K_{R1}}{100}\left(1-e^{\left(-\frac{N_{\mathrm{EFC}}-N_{\mathrm{EFC\_delay}}}{\tau_{R1}}\right)}\right)\right) \tag{8}$$

where $R_{1\mathrm{init}}$ is the initial value of the parameter R_1, K_{R1} is a dc gain in percent, τ_{R1} is a time constant, and N_{EFC} is a number of EFC, and $N_{\mathrm{EFC\_delay}}$ represents a time delay for EFC, from which the R_1 parameter starts to grow.

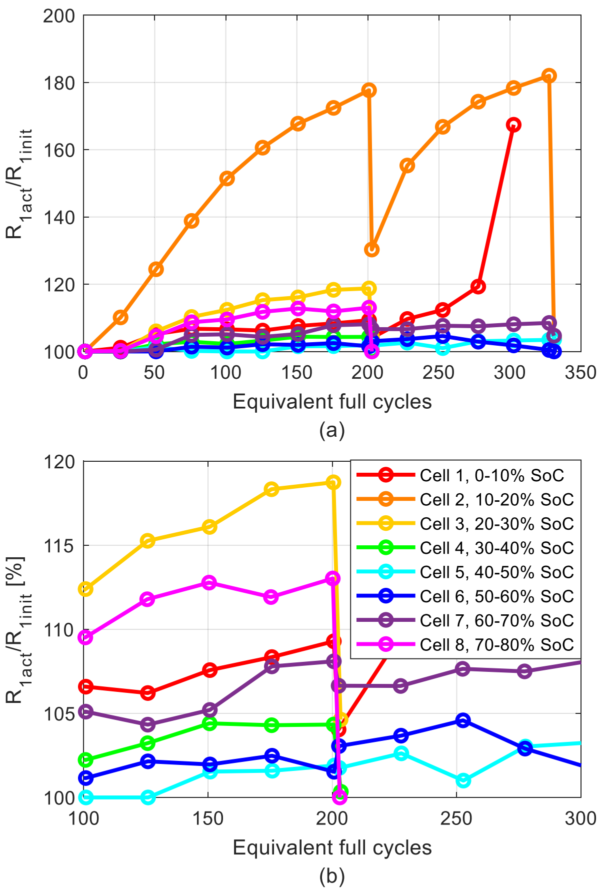

(a)

(b)

Fig. 17. Evolution of parameter R_1 (a) at 50% SoC for all cells with 10% ΔDoD and (b) detail in R_1 regeneration after 200 EFC.

Power fading can be caused by an increase of any resistance parameter in ECM, but since the R_1 parameter has a dominant role in power fading and is responsible for the regeneration phenomenon, we will refer to the R_1 parameter evolution as power fading and power regeneration.

To observe power fading across the whole SoC range, an evolution of parameter R_1 for Cell 1 to 8 is shown in Fig. 17. Capacity fading of these cells in Fig. 6 indicates power regeneration only for Cell 2, 3, and 8, however, a relatively significant drop in parameter R_1 was also recorded for Cell 1 and 4. Cell 2 experienced an enormous power fade compared to the rest of the cells with 10% ΔDoD. Therefore, a cycling SoC range plays a crucial role in power fading. Fit parameters of power fading for different SoC ranges are listed in Table IV.

As seen in Figs. 11 and 12, there is a correlation between the R_1 growth and the capacity fade, but the capacity fade in Fig. 12 contains also a linear part due to the SEI growth. We will therefore rewrite (1) as follows:

$$C_{\text{bat}} = C_{\text{init}} - \sum_{i=1}^{n} \Delta C_i - C_r \tag{9}$$

where C_r represents a capacity drop due to an increase in internal impedance including the regeneration phenomenon. As explained above, there is a correlation between the capacity fade and the R_1 evolution, therefore,

$$C_r = k_r \left(\frac{R_{1\text{act}}}{R_{1\text{init}}} - 1 \right) \tag{10}$$

where k_r represents the rate of capacity fade due to R_1 growth.

TABLE IV

Fit Parameters of Battery Model (Power Fading) for (8) and (10)

Cell no.	SoC_L	SoC_H	K_{R1}	N_{EFC_delay}	τ_{R1}	k_r
Cell 2	0.1	0.2	99.5	14.2	121.8	0.09
Cell 4	0.3	0.4	4.8	20.9	77.1	0
Cell 6	0.5	0.6	2.3	32.4	67.1	0
Cell 8	0.7	0.8	13.5	25.9	53.9	0.145
Cell 9	0.05	0.35	35.6	17.0	42.5	0.056
Cell10	0.2	0.5	61.7	25.5	181.3	0.148
Cell13	0.1	0.6	31.9	25.0	60.1	0.139
Cell14	0.2	0.7	54.1	21.9	147.6	0.173

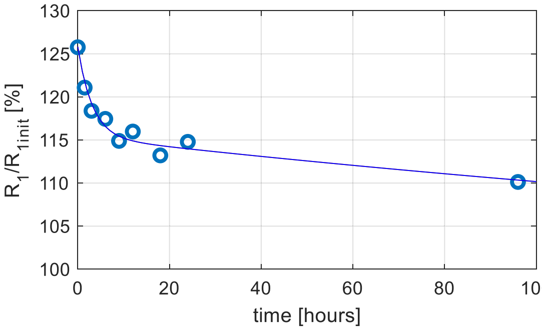

Fig. 18. Regeneration of parameter R_1 over time.

C. Power Regeneration Over Time and Its Modeling

Results in Fig. 15 indicate the resting period can effectively reduce power fading. However, an optimal time of resting when the most of power is regenerated was not clear. Furthermore, power regeneration over time is also important for modeling this phenomenon. Therefore, an additional cell was selected to observe the drop in the R_1 parameter value. The cell was cycled by the same schedule as Cell 14. The cell impedance was calculated by fitting the voltage response of the 6-min discharging pulse (0.5 C). The impedance was measured immediately after the cycling finish and after 1.5, 3, 6, 9, 12, 18, 24, and 96 h. The results are presented in Fig. 18. Right after the end of cycling, the R_1 parameter was 25.76% higher than the initial value, which is the R_1 value of a fresh cell.

The resistance drop was the most significant during the first 10 h. After 3 h, R_1 was 118.75% of its initial value, and after 9 h it was 114.89%. With further resting, only a very slow recovery was reported. The regeneration of parameter R_1 can be fit similarly to two RC pairs of ECM (23)

$$R_{1\text{act}} = R_{1\text{init}} + R_{1a} e^{-\frac{t}{\tau_{1a}}} + R_{1b} e^{-\frac{t}{\tau_{1b}}} \tag{11}$$

where R_{1a} and τ_{1a} are parameters related to the shorter time constant, and parameters R_{1b} and τ_{1b} of the longer

TABLE V
FIT PARAMETERS OF POWER REGENERATION

$R_{1a}[\Omega]$	$\tau_{1a}[h]$	$R_{1b}[\Omega]$	$\tau_{1b}[h]$	$R_{1init}[\Omega]$
0.0018	2.795	0.0027	220.773	0.0177

time constant. The shorter time constant describes fast power regeneration within the first 10 h and the longer time constant describes slow regeneration until R_1 drops to its initial value (see Fig. 18). Fit parameters of R_1 regeneration are shown in Table V.

In addition, (8) must be extended to include the power regeneration model. When the cell cycling is interrupted, an additional function takes part to estimate power regeneration. The power regeneration is calculated based on the power regeneration parameters in Table V, the actual $R_{1\mathrm{act}}$ value, and the resting time. The challenging part of power regeneration calculation is to estimate the actual R_{1a} and R_{1b} values since it depends on $R_{1\mathrm{act}}$. The increase of R_1 value due to power fading R_{1f} is calculated as follows:

$$R_{1f} = R_{1\mathrm{act}} - R_{1\mathrm{init}}. \tag{12}$$

R_{1f} is also a sum of R_{1a} and R_{1b} based on (11) at the beginning of the relaxation period ($t = 0$)

$$R_{1f} = R_{1a} + R_{1b}. \tag{13}$$

Therefore, the right ratio between R_{1a} and R_{1b} must be found. The ratio of R_{1a} within R_{1f} for the fit values in Table V is calculated as follows:

$$r = \frac{R_{1a}}{R_{1f}} = \frac{0.0018}{0.0018 + 0.0027} = 0.4. \tag{14}$$

Once we know the ratio r, R_{1b} is calculated as

$$R_{1b} = R_{1f}(1 - r). \tag{15}$$

However, τ_{1b} is a very long time constant and it takes several days until R_{1b} drops close to 0. If two resting periods were interrupted by only one charge-discharge cycle, the unregenerated part of R_{1b} would have not been taken into account for the new R_{1b} calculation in (15). Therefore, an unregenerated part of the resistance R_1 is introduced

$$R_{1\mathrm{ur}} = R_{1b} e^{-\frac{T_{\mathrm{rest}}}{\tau_{1b}}} \tag{16}$$

where T_{rest} is the length of the resting period in hours. If the newly calculated R_{1b} is smaller than $R_{1\mathrm{ur}}$ from the previous resting period, then R_{1b} will be set to $R_{1\mathrm{ur}}$.

If the value of R_{1b} is already known, then

$$R_{1a} = R_{1f} - R_{1b}. \tag{17}$$

Once the R_{1a_act} and R_{1b_act} are estimated, the new actual value $R_{1\mathrm{act}}$ after the resting period can be calculated

$$R_{1\mathrm{act}} = R_{1\mathrm{init}} + R_{1a\_\mathrm{act}} e^{-\frac{T_{\mathrm{rest}}}{\tau_{1a}}} + R_{1b\_\mathrm{act}} e^{-\frac{T_{\mathrm{rest}}}{\tau_{1b}}}. \tag{18}$$

After the resting period, a new N_{EFC} value must be calculated for the further $R_{1\mathrm{act}}$ calculations in (8). The $N_{\mathrm{EFC\_new}}$ value is also determined from (8)

$$N_{\mathrm{EFC\_new}} = N_{\mathrm{EFC\_delay}} - \tau_{R1} \ln\left(1 + \frac{R_{1\mathrm{init}} - R_{1\mathrm{act}}}{R_{1\mathrm{init}} \frac{K_{R1}}{100}}\right) \tag{19}$$

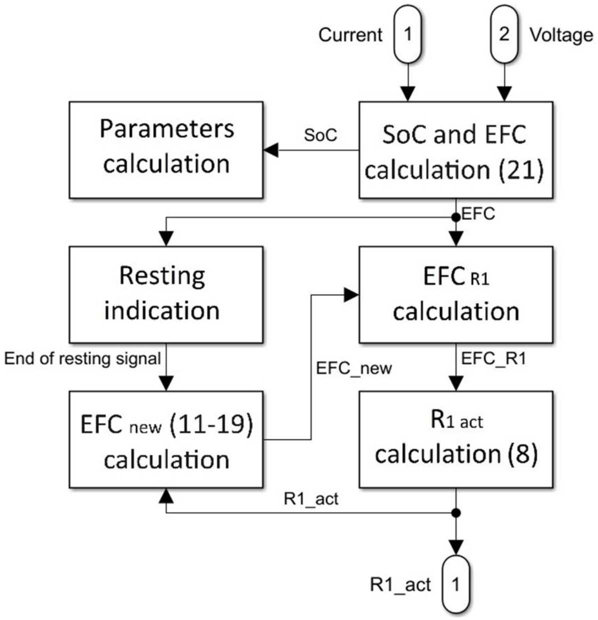

Fig. 19. Block diagram describing the interworking of the equations for the calculation of the parameter R_1.

TABLE VI
PARAMETERS OF THE POWER REGENERATION MODEL

R_{1init}	initial value of parameter R_1	R_{1a}, R_{1b}	Fitted parameters of the R_1 regeneration
R_{1act}	actual value of R_1	τ_{1a}, τ_{1b}	Fitted time constants of the R_1 regeneration
K_{R1}	DC gain of the R_1 growth	R_{1f}	Difference of R_{1act} and R_{1init}
τ_{R1}	time constant of the R_1 growth	r	The ratio of R_{1a} to R_{1f}
N_{EFC}	number of EFC	R_{1ur}	unregenerated part of the resistance R_1
N_{EFC_delay}	time delay of the R_1 growth	T_{rest}	Length of the resting period
k_r	rate of capacity fade due to R_1 growth	N_{EFC_new}	a new N_{EFC} value for the R_{1act} calculations

Based on (18) and (19), the new values of $R_{1\mathrm{act}}$ and N_{EFC} are calculated, and the model is able to predict R_1 regeneration. For a better understanding of how these equations work together, a block diagram is shown in Fig. 19. Based on the input current, the number of EFCs is calculated. $R_{1\mathrm{act}}$ is calculated from (8), where parameters K_{R1}, τ_{R1}, and $N_{\mathrm{EFC\_delay}}$ are determined from the SoC cycling range. Equations (12)–(19) are included in the EFC$_{\mathrm{new}}$ calculation block, which is activated only when the end of the resting period is detected. Then the new EFC value for $R_{1\mathrm{act}}$ calculation is set. All parameters of the power regeneration model are also organized in Table VI to increase readability.

D. Model Validation

Simulation results of the proposed model are depicted in Figs. 20–22. In Fig. 20, the measured evolution of R_1 is compared with simulation results. Simulation results of selected cells (dotted lines) show the prediction of the R_1

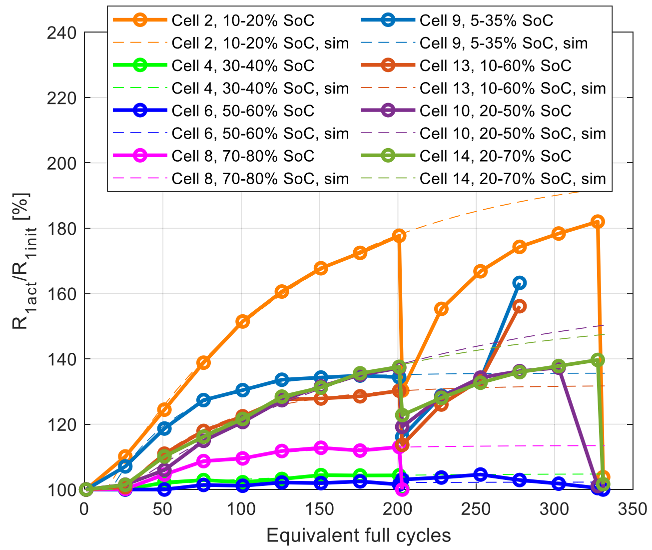

Fig. 20. Measured data of R_1 growth and simulation results.

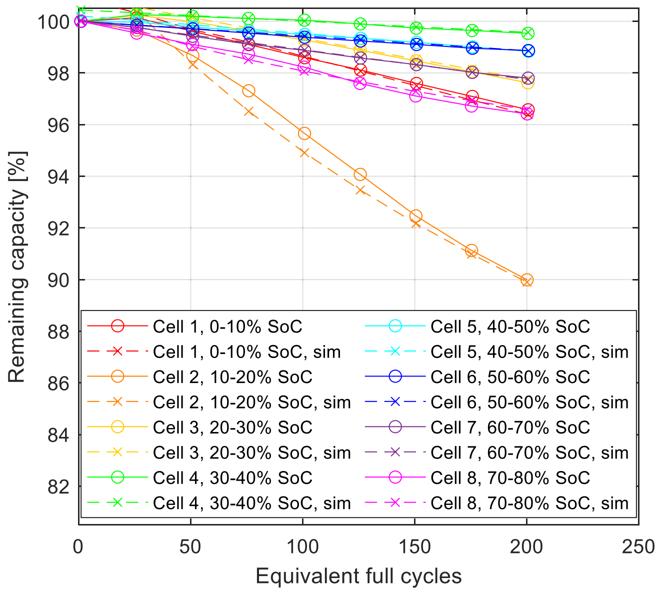

Fig. 21. Measured data of capacity fading and simulation results for ΔDoD $= 10\%$.

parameter if a resting period was not applied. After a resting period was applied, the R_1 value decreased, and subsequent cycling resulted in further power fading, which could also be modeled by a first-order system with time delay. In Fig. 21, measured and simulation results for cells cycled with ΔDoD $= 10\%$ are shown, and cells with ΔDoD $= 30\%$ and ΔDoD $= 50\%$ are shown in Fig. 22. To quantitatively evaluate the model accuracy, the RMSE was selected

$$\mathrm{RMSE} = \sqrt{\sum_{i=1}^{n} \frac{\left(C_{\mathrm{sim}(i)} - C_{\mathrm{mea}(i)}\right)^2}{n}} \tag{20}$$

where n is the number of data points, C_{sim} is the simulated cell capacity, and C_{mea} is the measured capacity. The model validated on our data had an RMSE of 1.26%. Therefore, the simulation results show a possibility of modeling battery cycling aging by the proposed model.

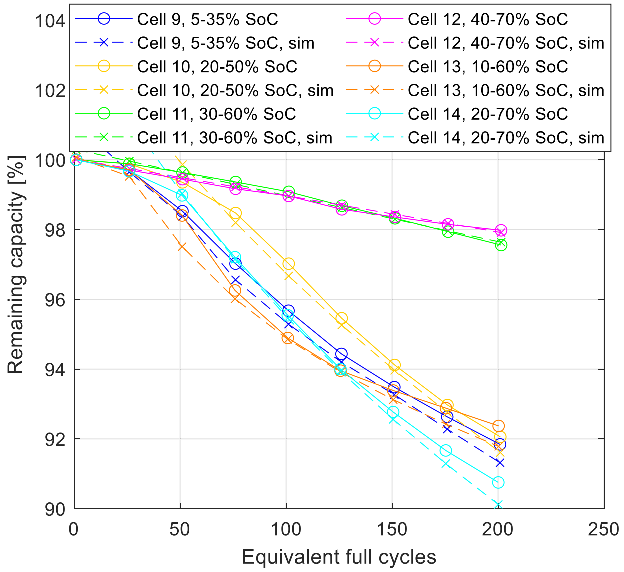

Fig. 22. Measured data of capacity fading and simulation results for ΔDoD $= 30\%$ and ΔDoD $= 50\%$.

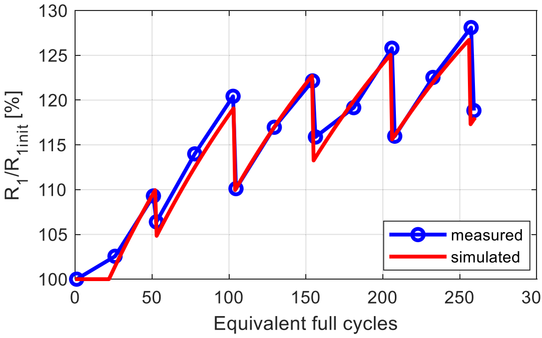

Fig. 23. Comparison of measured and simulated power regeneration for a cell cycled between 20–70% SoC with resting periods after every 50 EFC.

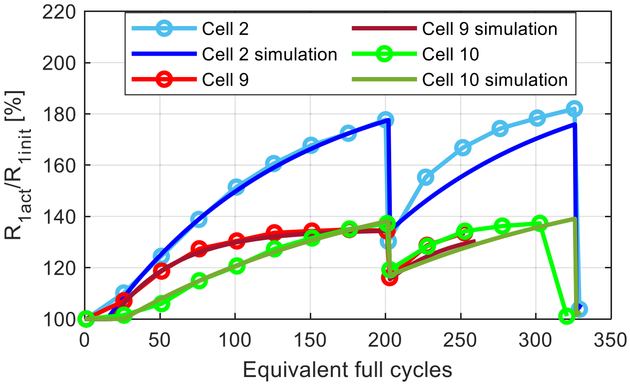

Fig. 24. Comparison of measured and simulated power regeneration for Cell 2, 9, and 10.

In Fig. 23, the measured results of a cell cycle between 20% and 70% SoC (discharging current of 3 C, charging current of 0.5 C) are compared with simulation results. The resting period of three days was applied after every 50 EFC. The figure shows this model can simulate the power regeneration phenomenon. The simulation results of the regeneration phenomenon for other SoC ranges can be seen in Fig. 24. The R_1 parameter resistance drop can be modeled with relatively high accuracy

TABLE VII
PARAMETERS OF BATTERY MODEL FOR NASA BATTERY DATASET SIMULATION

$R_{1a}[\Omega]$	$\tau_{1a}[h]$	$R_{1b}[\Omega]$	$\tau_{1b}[h]$	$R_{1init}[\Omega]$
0.0018	50	0.0027	3000	0.0177

SoC_L	SoC_H	K_{R1}	N_{EFC_delay}	τ_{R1}	k_r
0	1	600	13	25	0.0667

k_c	282e-6	k_d	2.6	k_e	1.222

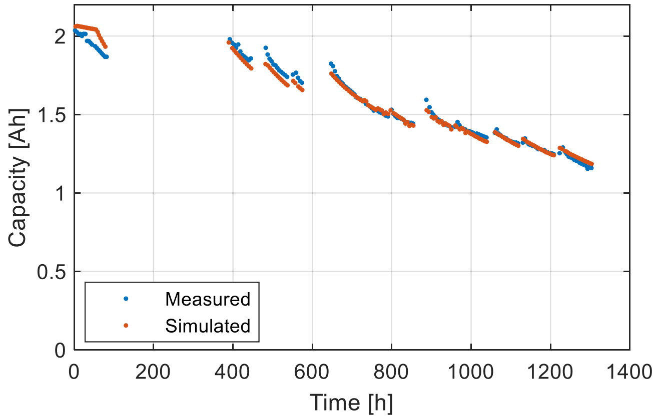

Fig. 25. Comparison of NASA dataset and simulation results.

even for longer resting periods. However, with further cycling, the R_1 parameter increases faster after the resting period for these cells, which was not visible for cells with more frequent resting periods. That indicates the τ_{R1} parameter gets shorter after resting periods. Nevertheless, the proposed model has great potential to improve the practical modeling of power fading and regeneration.

E. Model Validation on NASA Datasets

To demonstrate that the proposed model can be applied to model capacity regeneration on different types of battery cells, the NASA datasets were selected for model verification [46]. This dataset was often used for model validation in previous studies, so this gives us good legitimacy to use the same dataset for validation of the proposed model. Thus, the same cycling schedule was used in our simulation, and the input of the model was only the current profile and the constant temperature. The parameters used in the simulation for this cell are in Table VII. The simulation results and the NASA data of battery cell no. 06 are shown in Fig. 25. The RMSE calculated based on (20) was 3.82%.

The presented results show that the model can predict the impact of the internal impedance on discharge battery capacity. If low-frequency impedance parameters can be estimated, then the battery capacity after a resting period can be estimated based on the length of the resting period. That improves the SoH estimation as well as the vehicle range estimation.

V. CONCLUSION

In this article, NMC battery cell degradation is investigated, and the special focus is dedicated to the capacity regeneration phenomenon. It was shown that the capacity regeneration phenomenon is a consequence of varying internal impedance, and the biggest influence on capacity regeneration is the R_1 parameter of the ECM, which represents low-frequency diffusion. Thus, the reduced internal impedance results in the increased discharge capacity. The results of the R_1 growth during cycling show that it can be very well described by a first-order system with a time delay. On the other hand, the R_1 regeneration can be modeled by using two time constants. The R_1 parameter resistance drops significantly during the first 10 h of resting. If a long enough resting period is applied, which can take several days, the R_1 parameter drops down to its initial value of a fresh cell.

The experimental results show that the regeneration phenomenon is more prone to occur for specific SoC values. For example, it is the lowest at 30%–60% SoC, and the R_1 growth is negligible in this region. On the other hand, the R_1 growth is very significant, especially for too low SoC around 10%–25%, but also for high SoC (70%–80%). It occurs already at standard cycling conditions for INR18650-35E cell (charging current 0.5 C at 25 °C). Therefore, an explanation for the R_1 growth could be the larger concentration gradients within the electrode material due to mechanical strains during the cycling, which can explain the high SoC dependence. After a long resting time, concentration gradients become lower creating the regeneration phenomenon.

Since the R_1 parameter has the biggest influence on the capacity regeneration phenomenon, the internal impedance model must be included to model this phenomenon, which was not made in previous studies. A semi-empirical model considering these factors is presented in this article while maintaining low computational requirements. The R_1 estimation model is created as an extension of the capacity fading model due to SEI growth. The discharge capacity drop due to power fade is modeled to be proportional to the R_1 growth. The model was validated on the NASA battery datasets with an accuracy of 3.82%.

The proposed model can be applied in the advanced BMS systems in the future for more accurate capacity and power estimation. A charging strategy to reduce power fade can be also implemented considering factors influencing the impedance growth.

APPENDIX A
MOST SIGNIFICANT DEGRADATION MECHANISMS

The greatest influence on battery aging is the SEI growth and the lithium plating.

A. SEI Growth

The SEI is a protecting layer, which is formed at the anode surface during the first few cycles called formation. The anode of a Li-ion battery is usually made of graphite and its potential ranges from 0.3 to 0.0 V with respect to a lithium reference electrode (Li/Li^+) [47]. However, the electrolyte stability window is around 1–4.5 V for commonly used electrolytes [12] such as dimethyl carbonate or ethylene carbonate. Anode potential is out of this window, so the electrolyte solution is not thermodynamically stable and a reduction reaction takes place at the anode surface. Besides the protective function of SEI, it plays a significant role in battery aging. SEI continues growing during the whole lifetime of the battery even though it has a protective and self-passivating character. Changes in anode volume cause cracking of the SEI layer and the graphite is repeatedly exposed to react with the electrolyte, and that influences battery performance. SEI growth consumes available Li-ions and increases the internal impedance of the cell at the same time. The results are capacity fade, power fade, and lower energy efficiency. SEI growth occurs not only during cycling but also under storage conditions (calendar aging).

B. Lithium Plating

It occurs on the surface of the anode when charging with too high currents or when charging in cold conditions. Low temperatures lead to a decrease in the diffusion of lithium ions, which results in the lithium ions accumulation on the surface of the anode and lithium metal formation [48]. It also reduces the active surface of the anode, which increases the current density in other parts of the anode, thus the degradation is more and more accelerated [12]. The deposition of metallic lithium is initially reversible, and this lithium dissolution is known as lithium stripping. However, some part of the deposited lithium is irreversibly lost because of the reaction with the electrolyte or due to an electrical contact loss [41]. This process can destroy the cell within a few cycles. Fortunately, it can be effectively avoided by reducing charging currents at lower temperatures.

APPENDIX B
DEFINITIONS OF SOC, DOD, AND ΔDOD

The SoC is defined as a ratio of the available charge stored in a cell to the nominal capacity of the cell, it can be expressed as

$$\mathrm{SoC}(t) = \mathrm{SoC}(t_0) + \frac{1}{C_{\mathrm{bat}}}\int_{t_0}^{t} i_{\mathrm{bat}}(t)\eta_c(t)dt \tag{21}$$

where $\mathrm{SoC}(t_0)$ is the initial value of SoC, C_{bat} is the total battery capacity, i_{bat} is battery current, and η_c is the coulombic efficiency of the cell.

In the literature, the DoD is formulated as discharged capacity related to the nominal capacity [30]. However, in this article, the cells are cycled from lower initial values of SoC. Therefore, ΔDoD is defined as:

$$\Delta\mathrm{DoD} = \mathrm{SoC}_H - \mathrm{SoC}_L \tag{22}$$

where SoC_H is the higher limit of SoC during cycling and SoC_L is the lower limit for that specific cycle.

APPENDIX C
ECM PARAMETERS CALCULATION

The voltage response on a current pulse for the second-order ECM is described by the equation [30]

$$V_{\mathrm{bat}}(t) = V_{\mathrm{OCV}} - V_0 - V_1 e^{-\frac{t}{\tau_1}} - V_2 e^{-\frac{t}{\tau_2}} \tag{23}$$

where V_{OCV} is the open circuit voltage, V_0 is an instantaneous voltage drop across a series of internal resistance R_0, τ_1, and τ_2 are longer and shorter time constants, and V_1 and V_2 are voltage drops across each of RC pairs in a steady state.

Parameter identification described in [31] was adopted in this article. Parameters in (23) were extracted by curve fitting using the curve fitting toolbox in MATLAB. The ECM parameters were then calculated based on the following equations:

$$R_0 = \frac{V_0}{I} \tag{24}$$

$$R_i = \frac{V_i}{I} \tag{25}$$

$$C_i = \frac{\tau_i}{R_i} \tag{26}$$

where I is the current of the applied pulse. More details can be found in [31].

APPENDIX D
PHYSICAL PHENOMENA BEHIND CAPACITY FADING

For creating a semi-empirical model of capacity fading caused by SEI growth, a comprehension of physical phenomena happening inside the cell is needed.

A. SoC Effect

The battery cell experiences an anode volume expansion of 8% to 13% during charging and compression during discharging [49], [50]. This results in mechanical stress on the SEI layer, which can cause its cracking and subsequent repair. Therefore, the anode volume expansion plays a significant role in SEI growth.

The anode volume expansion was studied by Mohtat et al. in [49] and [50]. In [49], a relationship between electrode potential and volume expansion was shown. The anode volume expansion rate is the smallest between 30% and 70% SoC. A very similar relation of the volume expansion from SoC can be also found in [51] and [52]. This is also in line with experimental results in [14], where battery aging was the slowest around 50% SoC.

B. ΔDoD Effect

Another cause of SEI growth is the concentration gradient. During cycling, there can be large differences in lithium concentration within the electrode particles, causing diffusion within the particle and thus mechanical stress, which can cause the particle to crack [53], [54]. In the case of graphite cracking, a new anode surface on which a new SEI layer begins to form upon contact with the electrolyte. At higher temperatures, diffusion is relatively fast and lithium concentration gradients inside the particles are lower, so there is less chance of the electrode material cracking. Conversely, at lower temperatures, this risk is higher. Experimental studies show that graphite cracking is unlikely at 25 °C, even at a discharging current of 30 °C, so graphite particle cracking is unlikely in vehicular application [55]. However, the ΔDoD has still some impact on capacity fading due to SEI cracking, which was well explained in [54]. It follows from their model that the capacity loss caused by SEI cracking grows exponentially with ΔDoD.

C. C-Rate Effect

The impact of charging and discharging current on SEI growth was investigated in [56]. The authors concluded that SEI growth occurs nearly exclusively during battery charging. A strong dependence of SEI growth on charging C-rate was found, and it increases roughly linearly with the C-rate [56]. Similar observations were also found in [38], which showed that the SEI growth is suppressed during discharging, and directly proportional to intercalation current density during charging. In addition, C-rate also has an impact on the concentration gradient, meaning that from a certain value of C-rate, cracking of the electrode material can occur as described above. The C-rate also influences the temperature of the cell, since at higher C-rates there are greater losses, which are converted into heat, which accelerates side reactions.

D. Temperature Effect

The temperature has presumably the most significant effect on battery degradation and performance. EVs are therefore equipped with active thermal management, which controls the operating temperature of the battery pack. In general, the prevailing opinion is that the most suitable temperature for battery life during cycling is around 25 °C because high temperatures accelerate secondary chemical reactions, and charging at low temperatures can cause lithium plating. Moreover, the impedance of the cell increases at low temperatures, reducing the power and capacity of the cell. The effect of temperature on the SEI growth is modeled by the Arrhenius equation, which expresses the dependence of a chemical reaction on temperature [57], [48], [58]

$$A = A_0 e^{-\frac{E_a}{RT}} \tag{27}$$

where A_0 is a preexponential factor, E_a is the activation energy, which is the minimum required energy to undergo a chemical reaction, R stands for universal gas constant, and T is the temperature in kelvin.

REFERENCES

[1] A. Jossen, V. Spath, H. Doring, and J. Garche, "Battery management systems (BMS) for increasing battery life time," in *Proc. 21st Int. Telecommun. Energy Conf. (INTELEC)*, Jun. 1999, p. 56, doi: 10.1109/INTLEC.1999.794018.

[2] D. G. Elvira et al., "Simplified Li ion cell model for BMS coupling an equivalent circuit dynamic model with a zero dimensional physics based SEI model," *J. Electrochemical Soc.*, vol. 168, no. 11, Nov. 2021, Art. no. 110526, doi: 10.1149/1945-7111/ac3597.

[3] M. Tomasov, M. Kajanova, P. Bracinik, and D. Motyka, "Overview of battery models for sustainable power and transport applications," *Transp. Res. Proc.*, vol. 40, pp. 548–555, Jan. 2019, doi: 10.1016/j.trpro.2019.07.079.

[4] S. M. Mousavi G. and M. Nikdel, "Various battery models for various simulation studies and applications," *Renew. Sustain. Energy Rev.*, vol. 32, pp. 477–485, Apr. 2014, doi: 10.1016/j.rser.2014.01.048.

[5] J. Meng, G. Luo, M. Ricco, M. Swierczynski, D.-I. Stroe, and R. Teodorescu, "Overview of lithium-ion battery modeling methods for state-of-charge estimation in electrical vehicles," *Appl. Sci.*, vol. 8, no. 5, p. 659, Apr. 2018, doi: 10.3390/app8050659.

[6] G. Salda na, J. I. S. Martín, I. Zamora, F. J. Asensio, and O. Onederra, "Analysis of the current electric battery models for electric vehicle simulation," *Energies*, vol. 12, no. 14, p. 2750, Jul. 2019, doi: 10.3390/en12142750.

[7] W. Zhou, Y. Zheng, Z. Pan, and Q. Lu, "Review on the battery model and SOC estimation method," *Processes*, vol. 9, no. 9, p. 1685, Sep. 2021, doi: 10.3390/pr9091685.

[8] Y. Jia et al., "Parameter identification method for a fractional-order model of lithium-ion batteries considering electrolyte-phase diffusion," *Batteries*, vol. 8, no. 8, p. 90, Aug. 2022, doi: 10.3390/batteries8080090.

[9] J. Li, M. Mazzola, J. Gafford, and N. Younan, "A new parameter estimation algorithm for an electrical analogue battery model," in *Proc. 27th Annu. IEEE Appl. Power Electron. Conf. Expo. (APEC)*, Feb. 2012, pp. 427–433, doi: 10.1109/APEC.2012.6165855.

[10] X.-G. Yang, "Modeling of lithium plating induced aging of lithium-ion batteries: Transition from linear to nonlinear aging," *J. Power Sources*, vol. 360, pp. 28–40, Aug. 2017, doi: 10.1016/j.jpowsour.2017.05.110.

[11] J. Wang et al., "Degradation of lithium ion batteries employing graphite negatives and nickel–cobalt–manganese oxide + spinel manganese oxide positives: Part 1, aging mechanisms and life estimation," *J. Power Sources*, vol. 269, pp. 937–948, Dec. 2014, doi: 10.1016/j.jpowsour.2014.07.030.

[12] W. Vermeer, G. R. Chandra Mouli, and P. Bauer, "A comprehensive review on the characteristics and modeling of lithium-ion battery aging," *IEEE Trans. Transport. Electric.*, vol. 8, no. 2, pp. 2205–2232, Jun. 2022, doi: 10.1109/TTE.2021.3138357.

[13] I. Baghdadi, O. Briat, J.-Y. Delétage, P. Gyan, and J.-M. Vinassa, "Lithium battery aging model based on Dakin's degradation approach," *J. Power Sources*, vol. 325, pp. 273–285, Sep. 2016, doi: 10.1016/j.jpowsour.2016.06.036.

[14] M. Ecker et al., "Calendar and cycle life study of Li(NiMnCo)O_2-based 18650 lithium-ion batteries," *J. Power Sources*, vol. 248, pp. 839–851, Feb. 2014, doi: 10.1016/j.jpowsour.2013.09.143.

[15] J. Schmalstieg, S. Käbitz, M. Ecker, and D. U. Sauer, "A holistic aging model for Li(NiMnCo)O_2 based 18650 lithium-ion batteries," *J. Power Sources*, vol. 257, pp. 325–334, Jul. 2014, doi: 10.1016/j.jpowsour.2014.02.012.

[16] A. Eddahech, O. Briat, N. Bertrand, J.-Y. Delétage, and J.-M. Vinassa, "Behavior and state-of-health monitoring of Li-ion batteries using impedance spectroscopy and recurrent neural networks," *Int. J. Electr. Power Energy Syst.*, vol. 42, no. 1, pp. 487–494, Nov. 2012, doi: 10.1016/j.ijepes.2012.04.050.

[17] A. Eddahech, O. Briat, and J.-M. Vinassa, "Lithium-ion battery performance improvement based on capacity recovery exploitation," *Electrochimica Acta*, vol. 114, pp. 750–757, Dec. 2013, doi: 10.1016/j.electacta.2013.10.101.

[18] Z. Tong, J. Miao, J. Mao, Z. Wang, and Y. Lu, "Prediction of Li-ion battery capacity degradation considering polarization recovery with a hybrid ensemble learning model," *Energy Storage Mater.*, vol. 50, pp. 533–542, Sep. 2022, doi: 10.1016/j.ensm.2022.05.026.

[19] Y. Cui and Y. Chen, "Prognostics of lithium-ion batteries based on capacity regeneration analysis and long short-term memory network," *IEEE Trans. Instrum. Meas.*, vol. 71, pp. 1–13, 2022, doi: 10.1109/TIM.2022.3154003.

[20] W. Wu, R. Ma, J. Liu, M. Liu, W. Wang, and Q. Wang, "Impact of low temperature and charge profile on the aging of lithium-ion battery: Non-invasive and post-mortem analysis," *Int. J. Heat Mass Transf.*, vol. 170, May 2021, Art. no. 121024, doi: 10.1016/j.ijheatmasstransfer.2021.121024.

[21] B. Epding, B. Rumberg, H. Jahnke, I. Stradtmann, and A. Kwade, "Investigation of significant capacity recovery effects due to long rest periods during high current cyclic aging tests in automotive lithium ion cells and their influence on lifetime," *J. Energy Storage*, vol. 22, pp. 249–256, Apr. 2019, doi: 10.1016/j.est.2019.02.015.

[22] T. Qin, S. Zeng, J. Guo, and Z. Skaf, "State of health estimation of Li-ion batteries with regeneration phenomena: A similar rest time-based prognostic framework," *Symmetry*, vol. 9, no. 1, p. 4, Dec. 2016, doi: 10.3390/sym9010004.

[23] Q. Ma, Y. Zheng, W. Yang, Y. Zhang, and H. Zhang, "Remaining useful life prediction of lithium battery based on capacity regeneration point detection," *Energy*, vol. 234, Nov. 2021, Art. no. 121233, doi: 10.1016/j.energy.2021.121233.

[24] H. Meng, M. Geng, J. Xing, and E. Zio, "A hybrid method for prognostics of lithium-ion batteries capacity considering regeneration phenomena," *Energy*, vol. 261, Dec. 2022, Art. no. 125278, doi: 10.1016/j.energy.2022.125278.

[25] G. Lyu, H. Zhang, Y. Zhang, and Q. Miao, "An interpretable remaining useful life prediction scheme of lithium-ion battery considering capacity regeneration," *Microelectron. Rel.*, vol. 138, Nov. 2022, Art. no. 114625, doi: 10.1016/j.microrel.2022.114625.

[26] J. Zhang, Y. Jiang, X. Li, H. Luo, S. Yin, and O. Kaynak, "Remaining useful life prediction of lithium-ion battery with adaptive noise estimation and capacity regeneration detection," *IEEE/ASME Trans. Mechatronics*, vol. 28, no. 2, pp. 632–643, Apr. 2023, doi: 10.1109/TMECH.2022.3202642.

[27] W. Vermeer, M. Stecca, G. R. C. Mouli, and P. Bauer, "A critical review on the effects of pulse charging of Li-ion batteries," in *Proc. IEEE 19th Int. Power Electron. Motion Control Conf. (PEMC)*, Apr. 2021, pp. 217–224, doi: 10.1109/PEMC48073.2021.9432555.

[28] P. Kollmeyer, A. Hackl, and A. Emadi, "Li-ion battery model performance for automotive drive cycles with current pulse and EIS parameterization," in *Proc. IEEE Transp. Electrific. Conf. Expo (ITEC)*, Jun. 2017, pp. 486–492, doi: 10.1109/ITEC.2017.7993319.

[29] M.-K. Tran, A. DaCosta, A. Mevawalla, S. Panchal, and M. Fowler, "Comparative study of equivalent circuit models performance in four common lithium-ion batteries: LFP, NMC, LMO, NCA," *Batteries*, vol. 7, no. 3, p. 51, Jul. 2021, doi: 10.3390/batteries7030051.

[30] L. Lam, P. Bauer, and E. Kelder, "A practical circuit-based model for Li-ion battery cells in electric vehicle applications," in *Proc. IEEE 33rd Int. Telecommun. Energy Conf. (INTELEC)*, Oct. 2011, pp. 1–9, doi: 10.1109/INTLEC.2011.6099803.

[31] D. Cittanti, A. Ferraris, A. Airale, S. Fiorot, S. Scavuzzo, and M. Carello, "Modeling Li-ion batteries for automotive application: A trade-off between accuracy and complexity," in *Proc. Int. Conf. Electr. Electron. Technol. for Automot.*, Jun. 2017, pp. 1–8, doi: 10.23919/EETA.2017.7993213.

[32] Y. Yu et al., "Constructing accurate equivalent electrical circuit models of lithium iron phosphate and lead–acid battery cells for solar home system applications," *Energies*, vol. 11, no. 9, p. 2305, Sep. 2018, doi: 10.3390/en11092305.

[33] S.-J. Kwon, S.-E. Lee, J.-H. Lim, J. Choi, and J. Kim, "Performance and life degradation characteristics analysis of NCM LIB for BESS," *Electronics*, vol. 7, no. 12, p. 406, Dec. 2018, doi: 10.3390/electronics7120406.

[34] G. L. Plett, *Battery Management Systems: Battery Modeling*, vol. 1. Norwood, MA, USA: Artech House, 2015.

[35] T. Waldmann, R.-G. Scurtu, K. Richter, and M. Wohlfahrt-Mehrens, "18650 vs. 21700 Li-ion cells—A direct comparison of electrochemical, thermal, and geometrical properties," *J. Power Sources*, vol. 472, Oct. 2020, Art. no. 228614, doi: 10.1016/j.jpowsour.2020.228614.

[36] T. Waldmann et al., "Influence of cell design on temperatures and temperature gradients in lithium-ion cells: An in operando study," *J. Electrochemical Soc.*, vol. 162, no. 6, pp. A921–A927, Mar. 2015, doi: 10.1149/2.0561506jes.

[37] A. K. de Souza, G. Plett, and M. S. Trimboli, "Lithium-ion battery charging control using a coupled electro-thermal model and model predictive control," in *Proc. IEEE Appl. Power Electron. Conf. Expo. (APEC)*, Mar. 2020, pp. 3534–3539, doi: 10.1109/APEC39645.2020.9124431.

[38] L. von Kolzenberg, A. Latz, and B. Horstmann, "Solid–electrolyte interphase during battery cycling: Theory of growth regimes," *ChemSusChem*, vol. 13, no. 15, pp. 3901–3910, Aug. 2020, doi: 10.1002/cssc.202000867.

[39] J. Guo, Y. Li, J. Meng, K. Pedersen, L. Gurevich, and D.-I. Stroe, "Understanding the mechanism of capacity increase during early cycling of commercial NMC/graphite lithium-ion batteries," *J. Energy Chem.*, vol. 74, pp. 34–44, Nov. 2022, doi: 10.1016/j.jechem.2022.07.005.

[40] M. Petzl and M. A. Danzer, "Nondestructive detection, characterization, and quantification of lithium plating in commercial lithium-ion batteries," *J. Power Sources*, vol. 254, pp. 80–87, May 2014, doi: 10.1016/j.jpowsour.2013.12.060.

[41] C. von Lüders, J. Keil, M. Webersberger, and A. Jossen, "Modeling of lithium plating and lithium stripping in lithium-ion batteries," *J. Power Sources*, vol. 414, pp. 41–47, Feb. 2019, doi: 10.1016/j.jpowsour.2018.12.084.

[42] X. Lin, K. Khosravinia, X. Hu, J. Li, and W. Lu, "Lithium plating mechanism, detection, and mitigation in lithium-ion batteries," *Prog. Energy Combustion Sci.*, vol. 87, Nov. 2021, Art. no. 100953, doi: 10.1016/j.pecs.2021.100953.

[43] P. M. Attia et al., "Review—'Knees' in lithium-ion battery aging trajectories," *J. Electrochemical Soc.*, vol. 169, no. 6, Jun. 2022, Art. no. 060517, doi: 10.1149/1945-7111/ac6d13.

[44] M. Petzl, M. Kasper, and M. A. Danzer, "Lithium plating in a commercial lithium-ion battery—A low-temperature aging study," *J. Power Sources*, vol. 275, pp. 799–807, Feb. 2015, doi: 10.1016/j.jpowsour.2014.11.065.

[45] G. Plett, *Battery Management Systems, Equivalent-Circuit Methods*, vol. 2. Norwood, MA, USA: Artech House, 2015.

[46] NASA Ames Prognostics Center of Excellence. *Li-ion Battery Aging Datasets*. Accessed: Jan. 3, 2024. [Online]. Available: https://c3.ndc.nasa.gov/dashlink/resources/133/

[47] A. M. Colclasure, K. A. Smith, and R. J. Kee, "Modeling detailed chemistry and transport for solid-electrolyte-interface (SEI) films in Li–ion batteries," *Electrochimica Acta*, vol. 58, pp. 33–43, Dec. 2011, doi: 10.1016/j.electacta.2011.08.067.

[48] A. Barré, B. Deguilhem, S. Grolleau, M. Gérard, F. Suard, and D. Riu, "A review on lithium-ion battery ageing mechanisms and estimations for automotive applications," *J. Power Sources*, vol. 241, pp. 680–689, Nov. 2013, doi: 10.1016/j.jpowsour.2013.05.040.

[49] P. Mohtat, S. Lee, J. B. Siegel, and A. G. Stefanopoulou, "Towards better estimability of electrode-specific state of health: Decoding the cell expansion," *J. Power Sources*, vol. 427, pp. 101–111, Jul. 2019, doi: 10.1016/j.jpowsour.2019.03.104.

[50] P. Mohtat, S. Lee, V. Sulzer, J. B. Siegel, and A. G. Stefanopoulou, "Differential expansion and voltage model for Li-ion batteries at practical charging rates," *J. Electrochemical Soc.*, vol. 167, no. 11, Jan. 2020, Art. no. 110561, doi: 10.1149/1945-7111/aba5d1.

[51] P. Pietsch et al., "Quantifying microstructural dynamics and electrochemical activity of graphite and silicon-graphite lithium ion battery anodes," *Nature Commun.*, vol. 7, no. 1, p. 12909, Sep. 2016, doi: 10.1038/ncomms12909.

[52] A. S. Ho et al., "3D detection of lithiation and lithium plating in graphite anodes during fast charging," *ACS Nano*, vol. 15, no. 6, pp. 10480–10487, Jun. 2021, doi: 10.1021/acsnano.1c02942.

[53] J. Purewal, J. Wang, J. Graetz, S. Soukiazian, H. Tataria, and M. W. Verbrugge, "Degradation of lithium ion batteries employing graphite negatives and nickel–cobalt–manganese oxide + spinel manganese oxide positives: Part 2, chemical–mechanical degradation model," *J. Power Sources*, vol. 272, pp. 1154–1161, Dec. 2014, doi: 10.1016/j.jpowsour.2014.07.028.

[54] R. D. Deshpande and D. M. Bernardi, "Modeling solid-electrolyte interphase (SEI) fracture: Coupled mechanical/chemical degradation of the lithium ion battery," *J. Electrochemical Soc.*, vol. 164, no. 2, pp. A461–A474, Jan. 2017, doi: 10.1149/2.0841702jes.

[55] K. Takahashi and V. Srinivasan, "Examination of graphite particle cracking as a failure mode in lithium-ion batteries: A model-experimental study," *J. Electrochemical Soc.*, vol. 162, no. 4, pp. A635–A645, Jan. 2015, doi: 10.1149/2.0281504jes.

[56] P. M. Attia, S. Das, S. J. Harris, M. Z. Bazant, and W. C. Chueh, "Electrochemical kinetics of SEI growth on carbon black: Part I. Experiments," *J. Electrochemical Soc.*, vol. 166, no. 4, pp. E97–E106, Feb. 2019, doi: 10.1149/2.0231904jes.

[57] L. Lam and P. Bauer, "Practical capacity fading model for Li-ion battery cells in electric vehicles," *IEEE Trans. Power Electron.*, vol. 28, no. 12, pp. 5910–5918, Dec. 2013, doi: 10.1109/TPEL.2012.2235083.

[58] S. Käbitz et al., "Cycle and calendar life study of a graphite|$LiNi_{1/3}Mn_{1/3}Co_{1/3}O_2$ Li-ion high energy system. Part A: Full cell characterization," *J. Power Sources*, vol. 239, pp. 572–583, Oct. 2013, doi: 10.1016/j.jpowsour.2013.03.045.

Dávid Bodnár received the B.Sc. and M.Sc. degrees in electrical engineering from the Technical University of Kosice, Kosice, Slovakia, in 2019 and 2021, respectively, where he is currently pursuing the Ph.D. degree. He graduated with a thesis on the energy consumption prediction of electric midibus.

He was working at Delft University of Technology, Delft, The Netherlands, as a Guest Ph.D. Researcher. His research interests include the areas of battery modeling, energy storage systems, and energy management systems.

Gautham Ram Chandra Mouli (Member, IEEE) received the bachelor's degree from the National Institute of Technology Trichy, India, in 2011, the master's degree in electrical engineering from Delft University of Technology (TU Delft), Delft, The Netherlands, in 2013, and the Ph.D. degree for the development of a solar-powered V2G electric vehicle charger and developed charging algorithms (with PRE, ABB, and UT Austin) from TU Delft, in 2018.

From 2017 to 2019, he was a Post-Doctoral Researcher at TU Delft pursuing his research on power converters for EV charging, smart charging of EVs, and trolley buses. He is a tenured Assistant professor at the DC Systems, Energy Conversion and Storage Group, Department of Electrical Sustainable Energy, TU Delft. He is the Coordinator and a Lecturer for the Massive Open Online Course (MOOC) on Electric cars on edX.org with 200 000 learners from 175 countries. He is involved in many projects at the national and EU levels concerning electric mobility and batteries such as Flexinet, TULIPS, FLOW, Drive2X, and NEON. His current research interests include electric vehicles and charging, batteries, power electronics, and control for grid integration.

Dr. Mouli was awarded the Best Paper Prize in IEEE TRANSACTIONS ON INDUSTRIAL INFORMATICS in 2018, the Best Poster Prize at Erasmus Energy Forum 2016, The Netherlands, and the Best Paper Prize at the IEEE INDICON Conference 2009, India. It was awarded the "Most Significant Innovation in Electric Vehicles" Award from IDtechEx in 2018 and the "Best Tech Idea of 2018" by KIJK. He is the Vice-Chair of the IEEE Industrial Electronic Society Benelux chapter.

František Ďurovský received the M.Sc. and Ph.D. degrees in electrical engineering from the Technical University of Košice, Kosice, Slovakia, in 1983 and 1993, respectively.

He is currently an Associated Professor and the Deputy Head of the Department of Electrical Engineering and Mechatronics, Faculty of Electrical Engineering and Informatics, Technical University of Košice. His research interests include motion control, electrical drives in industrial and automotive applications and control, and simulation of mechatronic systems.

Pavol Bauer (Senior Member, IEEE) received the master's degree in electrical engineering from the Technical University of Kosice, Kosice, Slovakia, in 1985, and the Ph.D. degree from Delft University of Technology, Delft, The Netherlands, in 1995.

He is currently a Full Professor with the Department of Electrical Sustainable Energy, Delft University of Technology, and the Head of DC Systems, Energy Conversion and Storage Group. He was also a Professor at Brno University of Technology, Brno, Czech Republic, in 2008, and Delft University of Technology, in 2016. He has worked on many projects for industry concerning wind and wave energy, power electronic applications for power systems such as Smarttrafo and HVDC systems, projects for smart cities such as PV charging of electric vehicles, PV and storage integration, and contactless charging, and participated in several Leonardo da Vinci and H2020 EU projects as project partner (ELINA, INETELE, E-Pragmatic) and a Coordinator (PEMCWebLab.comEdipe, SustEner, Eranet DCMICRO). He published over 72 journals and almost 300 conference papers in my field (with H factor Google Scholar 43, Web of Science 20), he is an author or coauthor of eight books, holds four international patents, and organized several tutorials at international conferences.

Zian Qin (Senior Member, IEEE) received the B.Sc. degree from Beihang University, Beijing, China, in 2009, the M.Sc. degree from Beijing Institute of Technology, Beijing, in 2012, and the Ph.D. degree from Aalborg University, Aalborg, Denmark, in 2015, all in electrical engineering.

He is currently an Associate Professor with the Department of Electrical Sustainable Energy, Delft University of Technology, Delft, The Netherlands. In 2014, he was a Visiting Scientist at RWTH Aachen University, Aachen, Germany. He has more than 100 journals/conference papers, four book chapters, and two international patents, and he has worked on several European, Dutch national and industrial projects in these areas. His research interests include power quality and stability of power electronics-based grids, solid-state transformers, and battery energy storage.

Dr. Qin is the winner of the Excellent Innovation Award in second place, in the IEEE International Challenge in Design Methods for Power Electronics. He is Dutch National Representative in Cigre Working Group B4.101 on grid-forming energy storage systems. He is an Associate Editor of IEEE TRANSACTIONS ON INDUSTRIAL ELECTRONICS and IEEE JOURNAL OF EMERGING AND SELECTED TOPICS. He is a Distinguished Reviewer for the 2020 IEEE TRANSACTIONS ON INDUSTRIAL ELECTRONICS. He served as the Technical Program Chair of IEEE-PEDG 2024, IEEE-PEDG 2023, IEEE-ISIE 2020, and IEEE-COMPEL 2020.